applied sciences

MDPI

Article

Microwave Assisted Preparation of Barium Doped Titania (Ba/TiO_2) as Photoanode in Dye Sensitized Solar Cells

Awais Ahmad [1], Safia Khan [2], Mariam Khan [3], Rafael Luque [1,*], Mohammed Jalalah [4,5] and Mabkhoot A. Alsaiari [4,6,*]

1 Departamento de Quimica Organica, Universidad de Cordoba, Edificio Marie Curie (C-3), Ctra Nnal IV-A, Km 396, E14014 Cordoba, Spain
2 Department of Chemistry, Quaid-i-Azam University, Islamabad 43520, Pakistan
3 School of Applied Sciences and Humanity (NUSASH), National University of Technology, Islamabad 44000, Pakistan
4 Promising Centre for Sensors and Electronic Devices (PCSED), Advanced Materials and Nano-Research Centre, Najran University, Najran 11001, Saudi Arabia
5 Department of Electrical Engineering, Faculty of Engineering, Najran University, Najran 11001, Saudi Arabia
6 Empty Quarter Research Unit, Department of Chemistry, College of Science and Art in Sharurah, Najran University, Sharurah, Najran 11001, Saudi Arabia
* Correspondence: q62alsor@uco.es (R.L.); mamalsaiari@nu.edu.sa (M.A.A.)

Abstract: Pure TiO_2 and barium (0.5 wt%) doped TiO_2 (Ba/TiO_2) nanostructures have been synthesized via facile microwave irradiation method. The pure anatase phase of synthesized photoactive material was confirmed by X-ray diffraction. Ba doping in the TiO_2 host structure influenced the optical band gap as confirmed by UV-visible spectroscopy. The optical band gap increased from 3.21 eV for the TiO_2 to 3.26 eV for Ba/TiO_2. Morphological analysis of synthesized TiO_2 and Ba/TiO_2 was conducted using scanning electron microscopy. Energy dispersive X-ray spectroscopy confirmed the formation of Ba/TiO_2 and no impurities were observed. Electrochemical impedance spectroscopy showed that the charge transfer resistance increased for Ba/TiO_2, which reduced dark current creation in a dye-sensitized solar cell. The highest power conversion efficiency (3.24%) was achieved for Ba/TiO_2 photoanode compared to 2.1% for a pure TiO_2 photoanode-based device.

Keywords: photoanode; dye-sensitized solar cell; nanoparticles; microwave synthesis

Citation: Ahmad, A.; Khan, S.; Khan, M.; Luque, R.; Jalalah, M.; Alsaiari, M.A. Microwave Assisted Preparation of Barium Doped Titania (Ba/TiO_2) as Photoanode in Dye Sensitized Solar Cells. *Appl. Sci.* **2022**, *12*, 9280. https://doi.org/10.3390/app12189280

Academic Editor: Allen M. Barnett

Received: 25 November 2021
Accepted: 21 January 2022
Published: 16 September 2022

1. Introduction

Society needs green and cost-effective technologies for the energy sector owing to the global greenhouse effect and depletion of fossil fuels in recent years. Among all existing green energy technologies such as wind turbines, fuel cells, hydropower, tidal power, solar thermal and biomass, solar cells are considered among the most promising and prominent energy sources [1–5]. Dye-sensitized solar cells (DSSCs) constitute an advanced generation of solar cells that mimic natural photosynthesis. With fabrication techniques including solution processable methods, the use of cheap materials and decent power conversion efficiency (PCE), DSSCs are promising candidates for the conversion of solar light into electricity [6–8]. The highest PCE of 13% has been achieved in DSSCs by employing ruthenium as a light-absorbing material [9]. Techniques employed to improve the performance of DSSCs aim to minimize recombination of the photoinduced electron hole pair while improving the charge transfer rate of photo-generated electrons in the transparent conducting substrate [10]. Reducing the charge recombination and enhancing charge transfer can be achieved by optimizing the band gap of the semiconducting metal oxide (MOS). The MOS in a DSSC serves as a substrate for dye uplifting as well as provides a path for photoinduced charge generation [11,12].

TiO_2 nanostructures are one of the significant photoanode materials owing to their superior properties, including wide band gap, large surface area, non-toxicity, low cost

and high stability [13,14]. The morphology of MOS plays a significant role in DSSCs; therefore, a fine-tuned morphology is required to deliver improved PCE in the device [15]. The photocatalytic efficiency of TiO_2 is affected by its ability to respond to radiation (UV along with visible light), and thus could be improved by shifting its optical absorption from UV to the visible region. It has been observed that the photocatalytic efficiency of TiO_2 is enhanced by modifying its band gap with different dopants [16]. A variety of TiO_2 nano-compositions involving nanoparticles, carbon spheres, TiO_2 nanoparticle composites, TiO_2 micro tablets, hollow spheres, nanotube composites, and nano-fiber nanoparticle composites have been successfully synthesized and used as DSSC photoanode materials [17–20]. Doping with transition metals [21,22], rare-earth elements [23,24] and noble metals [25] into TiO_2 has been widely investigated to reduce TiO_2 particle size and improve its (photo)(electro)catalytic performance. Co-doping along with different doping agents including metal–nonmetal, nonmetal–nonmetal, and metal—metal synergistically improves the optical absorption towards the visible region and reduces the recombination process [26]. Cu-N, B-N, Fe-C, Fe-N, Ni-N, and V-N have been studied as co-dopants with TiO_2 [27–33]. Co-doping of TiO_2 with N-C has been reported to modify its band gap, enhancing its photocatalytic activity towards the visible spectrum [34]. Co-doping of titania nanowires with tungsten carbon improves their electrochemical activity towards the oxygen-evolution reaction (OER) [35]. Ag/V-TiO_2 was also studied to photo-catalyze the degradation of rhodamine B dye in aqueous solutions. These co-doped materials exhibited the highest photocatalytic activity in the UV-visible region [36], Similarly, it has also been previously reported that barium doping in TiO_2 nanoparticles using microwave irradiation increases the optical band gap and reduces the particle size of TiO_2 nanoparticles for microbiological activity [37]. Several studies have reported co-doping of TiO_2 to enhance its optoelectrical properties.

The present work deals with the preparation of TiO_2 and Ba/TiO_2 composites using a simple microwave irradiation method. Microwave-assisted swift heating has achieved substantial significance as an emerging and favorable method for one-pot preparation of different metal nanostructures. Structural, optical, morphological, elemental, and electrochemical behaviors of synthesized photoanodes materials are investigated by X-ray diffraction (XRD), UV-visible spectroscopy, scanning electron microscopy (SEM), energy dispersive spectroscopy (EDS), and electrochemical-impedance spectroscopy (EIS). Moreover, the photovoltaic performance of synthesized TiO_2 and Ba/TiO_2 photoanodes has been studied. Increasing the optical band gap and surface area of Ba/TiO_2 photoanodes led to a reduction of dark current and increased dye loading capacity [38]. DSSCs prepared using Ba/TiO_2 composite photoanode delivered a PCE of 2.34%.

2. Materials and Methods

2.1. Materials

Titanium (IV) isopropoxide TTIP (95% purity), ruthenium dye (N3 dye), polyethylene glycol (PEG), barium chloride and Triton X- 100 were purchased from Alfa Aesar Company India. Ethanol was purchased from Merck Company India. Chloroplatinic acid (99.9%) was purchased from Himedia Company India. All of these chemicals were utilized as received, without any further treatments. All of the solutions were prepared using deionized water (DI).

2.2. Preparation of TiO_2 and Ba/TiO_2 Photoanode

A facile microwave irradiation method was employed to prepare Ba $_{(0\cdot5)}TiO_2$ photoanode materials. An initial solution was prepared using 2 g of TTIP added with 60 mL of deionized water and stirred for 1 h at 100 °C. A separate solution was prepared using barium chloride dissolved in DI water. After that, both solutions were mixed and kept under stirring for 1 h at room temperature. The solution was kept under microwave irradiation for 5 min at 450 W. The advantage of using a microwave oven relates to a reduced synthesis time and energy consumption as compared to conventional heating. Microwaves provide homogeneous and rapid heating [39]. Afterwards, the obtained photoanode materials were

calcined at 500 °C for 1 h to enhance the crystalline nature of the photoanode material. The same procedure was adopted for the preparation of TiO_2 photoanode.

2.3. Photoanode Preparation

Fluorine-doped tin oxide (FTO) glass substrates were cleaned in a soap solution followed by distilled water and ethanol. Hereafter, the synthesized photoanode material was prepared using binder solutions of PEG and Triton X100. As prepared, Ba/TiO_2 was deposited onto FTO using the doctor blade technique. The coated substrate was sintered at 300°C for 1 h to evaporate the binder as well as to generate porosity in the materials. The sintered substrate was immersed into 0.5 mM of ruthenium dye solution for 24 h to absorb the dye molecule. A thin layer of platinum was deposited onto the FTO glass using 5 mM chloroplatinic acid via doctor blade technique. The photo-electrode was clamped (using binder clips) with the counter-electrode to produce a sandwich-type formation. The liquid redox electrolyte composed of 0.5M potassium iodide (KI) and 0.02 M iodine (I_2) dissolved in acetonitrile was filled between the photoelectrode and counter-electrode. The active surface area of the as-prepared DSSC was about 0.25 cm^2 and the cross-sectional area of TiO_2 and Ba/TiO_2, approx. 10 μm.

2.4. Characterization

X-Ray diffraction (PANalytical-X'pert Pro powder diffractometer λ = 1.54 Å using Cu Kα radiation) analysis was conducted to determine the crystal structure of the MOS with 2θ range values from 10° to 80°. The measurement was carried out by step size of 0.0170° up to four decimal accuracies. SEM (ZEIS EVO 18 instrument with 20 kV acceleration voltage and 1.30 K magnification) was used for the morphological studies of the of photoanode materials. UV-visible spectrophotometry (Perkin-Elmer-Lambda-35 spectrophotometer) was used to investigate the optical properties. EIS was conducted by VSP300 biological instrument with a 10 mV voltage amplitude in the frequency range of 1 MHz–1 Hz. The current voltage (I-V) measurement was observed by means of an electrochemical computer-controlled workstation as well as a SAN-EI solar-stimulator. A 150-watt xenon lamp was used as a light source with an AM 1.5 G filter and an intensity of 100 mW cm^{-2}.

3. Results and Discussions

3.1. Structural Analysis

XRD patterns of single TiO_2 as well as Ba/TiO_2 nanomaterials are displayed in Figure 1. The diffraction peaks of TiO_2 and Ba/TiO_2 nanomaterials at 2θ values were 25.09°, 37.65°, 47.89°, 53.89°, 55.07°, 62.40°, 70.04° and 75.00°, matching well with JCPDS data (21-1272) having (101), (004), (200), (105), (211), (204) crystal planes, respectively [26]. No other characteristic peaks were reflected in the XRD pattern. Hence, both samples exhibited tetragonal structure, and corresponding lattice constant values are shown in Table 1. In the case of Ba/TiO_2 nanomaterials, an increase in intensity was evidenced due to the incorporation of Ba^{2+} (1.42 nm) into the TiO_2 host lattice because the ionic radius of Ba^{2+} is greater than that of Ti^{4+} (0.74 nm), which resulted in an increase in crystallinity. This substitution caused lattice distortion, inflation of the TiO_2 nanocrystal, and internal stress due to Ba doping [40], which reduced nucleation growth (particle size controller) [41]. Another study showed that doping of substrates with Ba caused shrinkage of the crystallite size of modified nanomaterials [42].

Table 1. Structural parameters derived from XRD patterns of the synthesized TiO_2 and Ba/TiO_2 photoanode.

Photoactive Material	FWHM (2θ)	d-Spacing (Å)	Crystallite Size(D) (nm)	Lattice Constant (Å)		Unit Cell Volume V $(Å)^3$	Density (ρ) (g/cm^3)	Specific Surface Area (m^2/g)
				a = b	C			
TiO_2	0.568 ± 0.026	3.494	25	3.778 ± 0.005	9.480 ± 0.012	135.31	3.9	61
Ba/TiO_2	0.876 ± 0.038	3.504	16	3.781 ± 0.002	9.470 ± 0.004	135.38	3.9	95

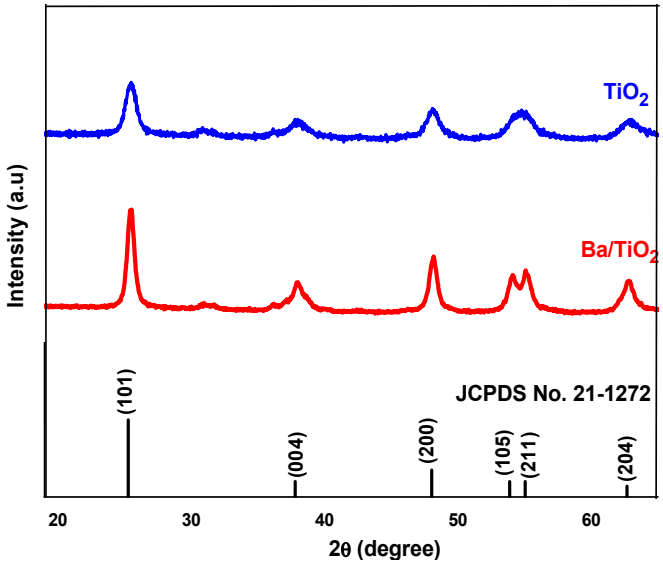

Figure 1. XRD patterns of Ba/TiO_2, TiO_2 photoanodes along with the reference JCPDS data 21-1272.

The structural constraints of synthesized TiO_2 and Ba/TiO_2 nanomaterials were calculated using the following formulas [43]:

$$\frac{1}{d^2} = \frac{h^2 + k^2}{a^2} + \frac{l^2}{c^2} \quad (1)$$

$$t = \frac{0.9\lambda}{\beta \cos\theta} \quad (2)$$

where d is the d-spacing between two consecutive lattices observed from XRD, (h,k,l) indicate the miller indices, t is the crystallite size, β is the full with half maximum, a, b, and c display as lattice constant for $a = b$ in tetragonal structure, λ indicates the wavelength of the X-ray radiation used, and θ refers to the diffraction angle;

$$\rho = \frac{nM}{NV} \quad (3)$$

$$S_a = \frac{6}{D.\rho} \quad (4)$$

where, ρ is the density of the prepared sample, n is 4 for anatase phase TiO_2 and 2 for rutile phase TiO_2, M is the molecular weight of the prepared nanomaterials, N corresponds to Avogadro's constant value, V is the volume of the prepared nanomaterials, and Sa states the specific surface of the prepared sample. Table 1 shows the calculated structural values derived from the XRD patterns of TiO_2 and Ba/TiO_2 nanomaterials. The average crystallite sizes estimated were 25 nm for single TiO_2 and 16 nm for Ba/TiO_2 nanomaterials, respectively. When Ba ions were doped into the TiO_2 lattice, a decrease in nucleation (and subsequent growth rate) was observed for TiO_2 nanomaterials, leading to a reduction in particle size of Ba/TiO_2. The reduction in particle size increases the surface area of TiO_2. The specific surface area of TiO_2 (61 m^2/g) was smaller than that of Ba/TiO_2 (95 m^2/g). This favored dye adsorption in the photo electrode, thereby improving photovoltaic performance in the DSSC.

3.2. Optical Properties

Figure 2 represents the UV-visible spectra of TiO_2 and Ba/TiO_2 photoanode materials. Ba/TiO_2 exhibited a significant visible absorption above 400 nm, which was an indication of changes occurring in the optical absorption of TiO_2 photoanode material due to metal doping. Peak edges of Ba/TiO_2 photoanode showed some regular and trivial blue shifts

comparative to TiO_2 photoanode. The blue shift was attributable to the Burstein–Moss effect, leading to the movement of Fermi level towards the conduction band due to an increase in electron concentration because of Ba doping [44,45]. It is very useful to increase the photocurrent density and also the charge transfer resistance of synthesized photoanodes. The absorption of TiO_2 and Ba/TiO_2 were at 415 nm and 400 nm, respectively.

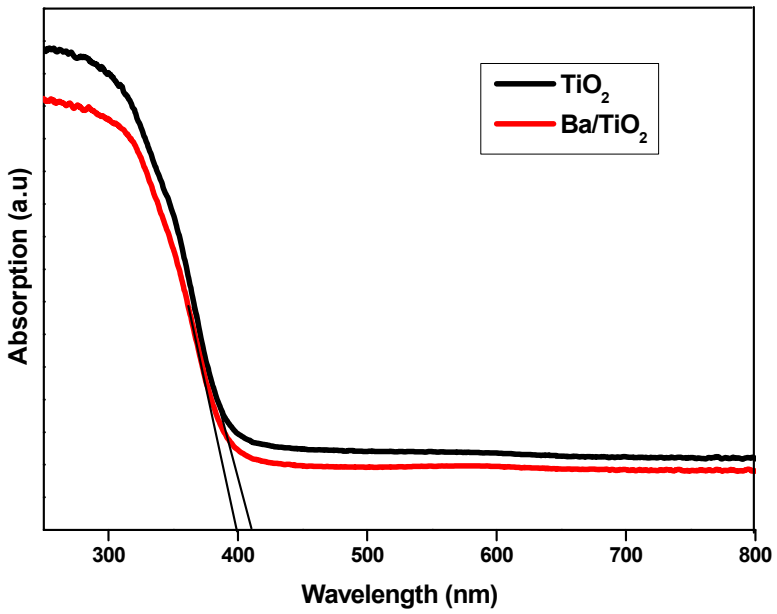

Figure 2. UV-visible spectra of synthesized TiO_2 and Ba/TiO_2 photoanodes.

Optical band gap values were determined by using Tauc plots as presented in Figure 3a. Ba/TiO_2 photoanode (3.26 eV) ha a higher band gap value compared to TiO_2 photoanode (3.21 eV) because of quantum confinement effects observed due to the smaller size of as-synthesized samples. According to the theory of quantum efficiency, the holes of valence band and conduction band electrons are confined by the potential barrier of the surface. As a result, the band gap energy is increased with decreasing size of synthesized particles [46,47]. The increase in band gap of doped TiO_2 can be interpreted in terms of Mott's transition effect and Burstein–Moss (BM) effects. According to Mott' criteria, the band gap of the donor combines with the conduction band of the host material [48], while BM effects present a relationship between the band gap and concentration of carriers [49,50], as given below:

$$E_g^{BM} = \left(\frac{h^2}{2\lambda m_e}\right)\left(3\pi^2 N_e\right) \quad (5)$$

where λ, h, and m_e are the effective reduced mass of TiO_2, Planck's constant and the electron free mass, respectively. According to the *BM* effect, the carrier density of semiconductors increases with Ba doping, which causes the Fermi level to shift into the conduction band [51]. Due to this doping, the low energy transition is clogged, and broadening in the band gap takes place [52]. This novel effect of Ba doping on optical properties can pave the way to its extended use in optoelectronic and photovoltaic applications.

The value of n coefficient is determined by the Tauc relationship (Equation (6)). The n coefficient is related to the possible transition of electrons. For indirect allowed electronic transition, its value is 2 and 3 for indirect forbidden transitions.

$$\alpha h\theta = A\,(h\theta - E_g)^n \quad (6)$$

$$n = \frac{ln\,(\alpha h\theta)}{\ln(h\theta - E_g)} \quad (7)$$

where α is the absorption coefficient, h is Plank's constant, and A is absorption constant [53]. From the slope of ln F® vs. ln $(-\nu - E_g)$, the value of n is determined. The result listed in Table 2 represents the approximated value of $n = 2$ for TiO_2 and Ba/TiO_2, which is in agreement with values in the literature for TiO_2, which is an indirect semiconductor [54]

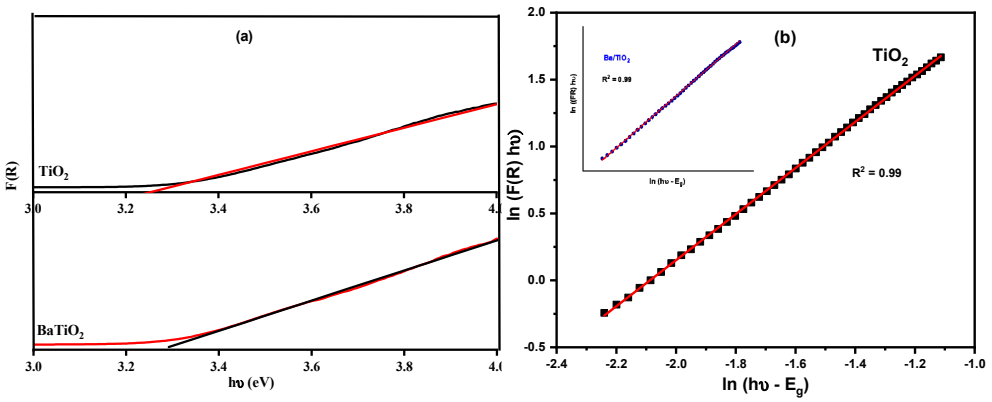

Figure 3. (**a**) Tauc plots of synthesized TiO_2 and Ba/TiO_2 photoanodes (**b**) Graphical representation of Equation (7), inset relates to Ba/TiO_2.

Table 2. n coefficient determination and band gap.

Sample	E_g (eV)	n Coefficient
TiO_2	3.21	1.72 ± 0.003
Ba/TiO_2	3.26	1.61 ± 0.003

Figure 4 presents the UV-visible absorption spectrum of dye molecule-adsorbed TiO_2 and Ba/TiO_2 photoanodes. The Ba/TiO_2 photoanode had high absorption compared to the TiO_2 photoanode. The increased absorption was due to the increasing surface area of the Ba/TiO_2 photoanode, which was also confirmed by XRD results. This behavior enhances photocurrent density in DSSCs. Moreover, the shift in wavelength in the visible region further supported our findings as productive in DSSCs, because the photocatalytic efficiency of TiO_2 is affected by its ability to respond to UV radiation along with visible light, which could be improved by shifting its optical absorption from UV to the visible region. Ba doping increased the absorption in the visible region.

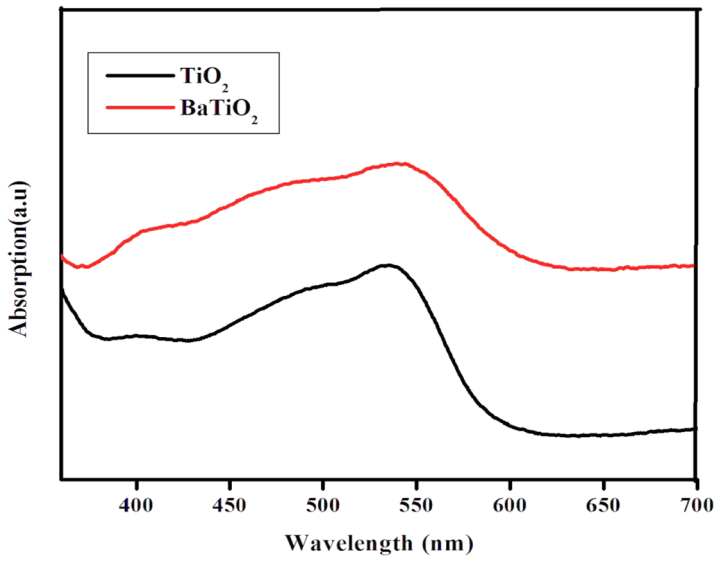

Figure 4. UV-visible absorption spectra of synthesized TiO_2 and Ba/TiO_2 photoanodes with N3 dye molecule.

3.3. Morphological Studies

The surface morphologies of the TiO_2 and Ba/TiO_2 nanostructures were subsequently examined by SEM as shown in Figure 5. Both TiO_2 (5a) and Ba/TiO_2 (5b) exhibited similar agglomerated spherical shape particles. In terms of chemical composition, TiO_2 nanostructures contained Ti and O, only, which confirmed that the material was free from impurities, as observed from Figure 5c. The presence of Ba was confirmed in the Ba/TiO_2 nanostructures from Figure 5d.

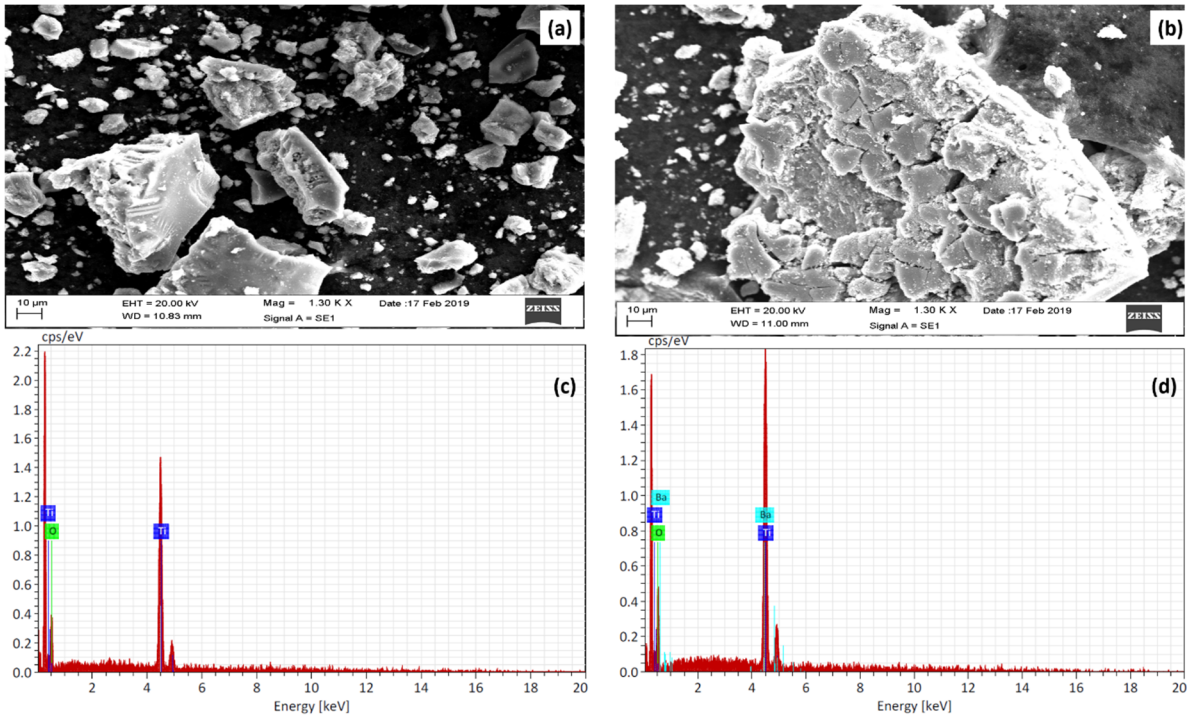

Figure 5. SEM analysis of synthesized (**a**) TiO_2 and (**b**) Ba/TiO_2, and EDS analysis of synthesized (**c**) TiO_2 and (**d**) Ba/TiO_2 nanopowders.

3.4. Electrochemical Behavior of TiO_2 and Ba/TiO_2

The reaction kinetics linked with DSSCs were investigated using EIS results. EIS spectra of TiO_2 and Ba/TiO_2 photoanodes under dark conditions with 0.6 V open circuit voltage are depicted in Figure 6. The EIS of DSSC was explained by three semicircles in the high, middle, and low frequency range, corresponding to the electrochemical output in platinized counter-electrode and electrolyte-interface (R_1), WE/electrolyte (R_2), and diffusion resistance of electrolyte (R_d), respectively. The displacement of the graph from origin represents the series resistance due to the contact resistance of the cell (R_s) [55]. Associated charge transfer in the electrolyte influenced the low frequency region, which was evident from the third semicircle. From the fitted data, the Ba/TiO_2 photoanode charge transfer resistance value was higher than the TiO_2 photoanode charge transfer resistance value. Barium doping increased the band gap value (which was also confirmed by optical analysis), and this reduces electron recombination in the Ba/TiO_2/electrolyte interface. This behavior is attributed to the charge transfer value increment. The increment of charge transfer resistance was helpful to reduce charge recombination, which was evident for the photocurrent increment.

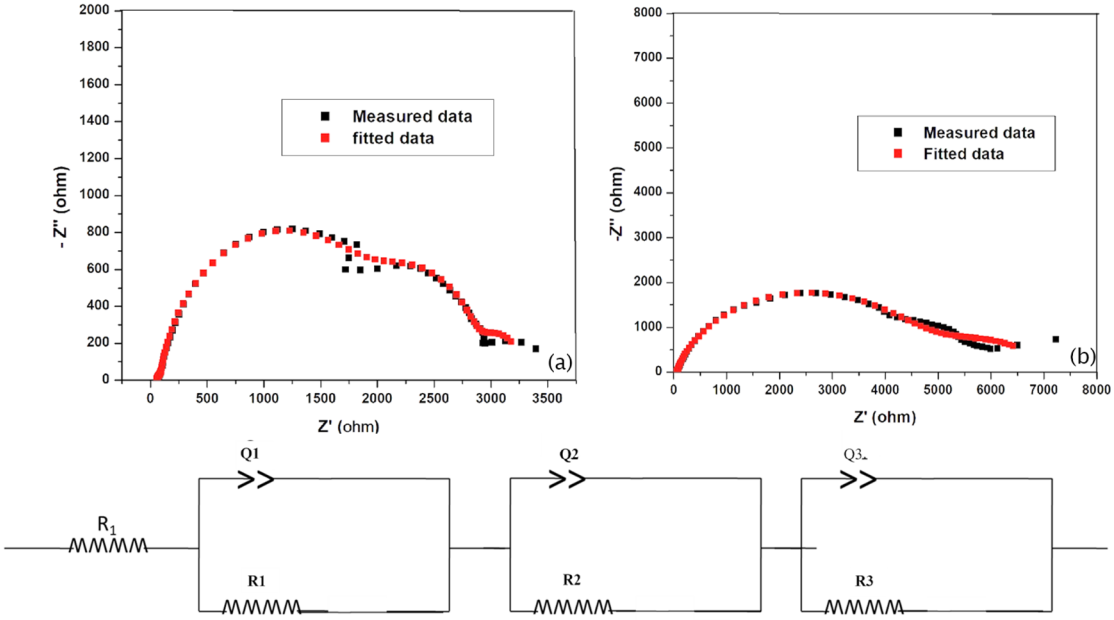

Figure 6. EIS analysis of synthesized (**a**) TiO_2, (**b**) Ba/TiO_2 photoanode and along with the equivalent circuit of corresponding EIS.

3.5. Photovoltaic Studies

The photovoltaic performance of the fabricated DSSC is shown in Figure 7. Photocurrent density of Ba/TiO_2 was higher than that of the TiO_2 photoanode. This increment was due to the increased photon absorption of dye molecule as compared to the TiO_2 counterpart. The Ba/TiO_2 photoanode had higher surface area than the TiO_2 photoanode, which led to enhanced dye-loading capacity. These results were also confirmed by the XRD and UV analysis. Another important factor was that the increment in photocurrent density was supported by the recombination rate or dark current reduction. The Ba/TiO_2 photoanode had the high recombination resistance compared to the TiO_2 photoanode, which reduce dark current production between the MOS and electrolyte.

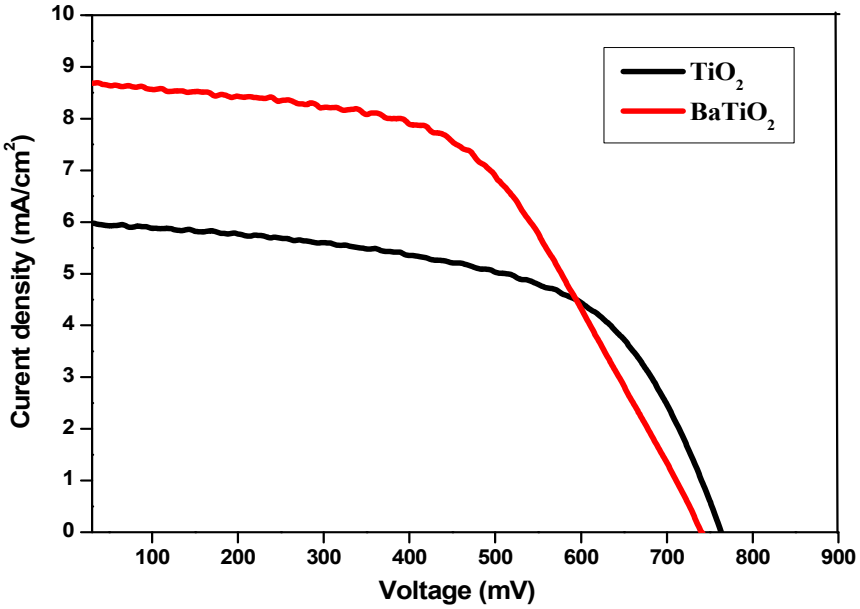

Figure 7. Photovoltaic response of synthesized TiO_2 and Ba/TiO_2 photoanodes.

The Ba/TiO_2 photoanode yielded higher PCE (3.4%) compared to the TiO_2 photoanode (2.1%). The calculated photovoltaic parameters are summarized in Table 3. The higher PCE of the Ba/TiO_2 photoanode (3.4%) corresponds to a maximum output power density (P_{max}) of approximately 34.4 $\mu W/cm^2$ as compared to the TiO_2 photoanode's P_{max} of 26.5 $\mu W/cm^2$. These findings suggest that DSSCs can be produced with the appropriate power rating to operate electronic devices such as tablets and Internet-of-Things gadgets that require low power $P_{max} < 100$ $\mu W/cm^2$ [56].

Table 3. Photovoltaic parameters derived from current voltage characteristic curves of synthesized TiO_2 and Ba/TiO_2 photoanodes.

Sample	Short Circuit Current Density J_{sc} (mA/cm^2)	Open Circuit Voltage V_{oc} (mV)	Fill Factor FF (%)	Efficiency (η) (%)	Ref
TiO_2	5.96	761	48	2.1	Present work
Ba/TiO_2	8.70	740	53	3.4	Present work
TiO_2	2.53	650	63	1.03	[57]
$W\text{-}TiO_2$	4.77	730	71	2.47	[57]
$Fe\text{-}TiO_2$	1.52	680	0.463	0.47	[26]

4. Conclusions

Incorporation of barium (0.5 wt%) into TiO_2 was successfully accomplished using a microwave irradiation method. With respect to Ba content, its incorporation modulated the band gap of TiO_2 by decreasing particle size, leads to increased specific surface area and consequently, superior dye uptake and high photocurrent, resulting in higher DSSC power conversion efficiency. The higher band gap value of Ba/TiO_2 (3.26 eV) as compared to TiO_2 photoanode (3.21 eV) was attributable to the quantum confinement effect, which was observed due to the reduced size of the as-synthesized samples. EDS results confirmed the presence of barium in Ba/TiO_2 without any impurities; this was further confirmed by XRD results. A higher efficiency of Ba/TiO_2 photoanode was observed as compared to pure TiO_2 (3.4 vs 2.1%). Barium doped titania (Ba/TiO_2) could be employed in DSSCs owing to its relevant photoactive properties, with further prospects for other applications including photocatalysis as well as wastewater treatment.

Author Contributions: Conceptualization, A.A. and S.K.; methodology, M.K.; software, M.K.; validation, M.K.; writing—original draft preparation, A.A.; writing—review and editing, R.L.; visualization, M.J.; supervision, R.L.; project administration, M.A.A.; funding acquisition, M.A.A. All authors have read and agreed to the published version of the manuscript.

Funding: This work was funded by Najran University, and the grant number is NU/IFC/INT/01/003.

Institutional Review Board Statement: Not applicable.

Informed Consent Statement: Not applicable.

Acknowledgments: The authors would like to acknowledge the support of the deputy for research and innovation-Ministry of Education, Kingdom of Saudi Arabia for this research through grant (NU/IFC/INT/01/003) under the institutional funding committee at Najran University, Kingdom of Saudi Arabia.

Conflicts of Interest: The authors declare no conflict of interest.

References

1. Perera, F. Pollution from fossil-fuel combustion is the leading environmental threat to global pediatric health and equity: Solutions exist. *Int. J. Environ. Res. Public Health* **2018**, *15*, 16. [CrossRef] [PubMed]
2. Khan, S.; Shah, S.S.; Anjum, M.A.R.; Khan, M.R.; Janjua, N.K. Electro-oxidation of ammonia over copper oxide impregnated γ-Al2O3 nanocatalysts. *Coatings* **2021**, *11*, 313. [CrossRef]
3. Tiewsoh, S.L.; Jirásek, J.; Sivek, M. Electricity generation in India: Present state, future outlook and policy implications. *Energies* **2019**, *12*, 1361. [CrossRef]

4. Khan, M.; Janjua, N.K.; Khan, S.; Qazi, I.; Ali, S.; Saad Algarni, T. Electro-oxidation of ammonia at novel Ag_2O-PrO_2/γ-Al_2O_3 catalysts. *Coatings* **2021**, *11*, 257. [CrossRef]
5. Saleem, M.; Irfan, M.; Tabassum, S.; Albaqami, M.D.; Javed, M.S.; Hussain, S.; Pervaiz, M.; Ahmad, I.; Ahmad, A.; Zuber, M. Experimental and theoretical study of highly porous lignocellulose assisted metal oxide photoelectrodes for dye-sensitized solar cells. *Arab. J. Chem.* **2021**, *14*, 102937. [CrossRef]
6. Ansir, R.; Shah, S.M.; Ullah, N.; Hussain, M.N. Performance of pyrocatechol violet and carminic acid sensitized ZnO/CdS nanostructured photoactive materials for dye sensitized solar cell. *Solid-State Electron.* **2020**, *172*, 107886. [CrossRef]
7. Jacobson, M.Z.; Delucchi, M.A. Providing all global energy with wind, water, and solar power, Part I: Technologies, energy resources, quantities and areas of infrastructure, and materials. *Energy Policy* **2011**, *39*, 1154–1169. [CrossRef]
8. Irvine, S. Solar Cells and Photovoltaics. In *Springer Handbook of Electronic and Photonic Materials*; Springer: Cham, The Netherlands, 2017; p. 1.
9. Gul, M.; Kotak, Y.; Muneer, T. Review on recent trend of solar photovoltaic technology. *Energy Explor. Exploit.* **2016**, *34*, 485–526. [CrossRef]
10. Sharma, K.; Sharma, V.; Sharma, S. Dye-sensitized solar cells: Fundamentals and current status. *Nanoscale Res. Lett.* **2018**, *13*, 381. [CrossRef]
11. Bose, S.; Soni, V.; Genwa, K. Recent advances and future prospects for dye sensitized solar cells: A review. *Int. J. Sci. Res. Publ.* **2015**, *5*, 1–8.
12. Mátravölgyi, B.; Hergert, T.; Thurner, A.; Varga, B.; Sangiorgi, N.; Bendoni, R.; Zani, L.; Reginato, G.; Calamante, M.; Sinicropi, A.; et al. Synthesis and Investigation of Solar-Cell Photosensitizers Having a Fluorazone Backbone. *Eur. J. Org. Chem.* **2017**, *2017*, 1843–1854. [CrossRef]
13. Yu, Q.; Pang, Y.; Jiang, Q. NiS submicron cubes with efficient electrocatalytic activity as the counter electrode of dye-sensitized solar cells. *R. Soc. Open Sci.* **2018**, *5*, 180186. [CrossRef] [PubMed]
14. Carella, A.; Borbone, F.; Centore, R. Research progress on photosensitizers for DSSC. *Front. Chem.* **2018**, *6*, 481. [CrossRef] [PubMed]
15. Mishra, A.; Fischer, M.K.; Bäuerle, P. Metal-free organic dyes for dye-sensitized solar cells: From structure: Property relationships to design rules. *Angew. Chem. Int. Ed.* **2009**, *48*, 2474–2499. [CrossRef] [PubMed]
16. Momeni, M.M. Dye-sensitized solar cell and photocatalytic performance of nanocomposite photocatalyst prepared by electrochemical anodization. *Bull. Mater. Sci.* **2016**, *39*, 1389–1395. [CrossRef]
17. Su'ait, M.S.; Rahman, M.Y.A.; Ahmad, A. Review on polymer electrolyte in dye-sensitized solar cells (DSSCs). *Sol. Energy* **2015**, *115*, 452–470. [CrossRef]
18. Wang, H.; Hu, Y.H. Graphene as a counter electrode material for dye-sensitized solar cells. *Energy Environ. Sci.* **2012**, *5*, 8182–8188. [CrossRef]
19. Labat, F.; Ciofini, I.; Hratchian, H.P.; Frisch, M.J.; Raghavachari, K.; Adamo, C. Insights into working principles of ruthenium polypyridyl dye-sensitized solar cells from first principles modeling. *J. Phys. Chem. C* **2011**, *115*, 4297–4306. [CrossRef]
20. Corrao, R.; D'Anna, D.; Morini, M.; Pastore, L. DSSC-integrated Glassblocks for the construction of Sustainable Building Envelopes. In *Advanced Materials Research*; Trans Tech Publ: Zurich, Switzerland, 2014.
21. Wu, C.-G.; Chao, C.-C.; Kuo, F.-T. Enhancement of the photo catalytic performance of TiO_2 catalysts via transition metal modification. *Catal. Today* **2004**, *97*, 103–112. [CrossRef]
22. Inturi, S.N.R.; Boningari, T.; Suidan, M.; Smirniotis, P.G. Visible-light-induced photodegradation of gas phase acetonitrile using aerosol-made transition metal (V, Cr, Fe, Co, Mn, Mo, Ni, Cu, Y, Ce, and Zr) doped TiO_2. *Appl. Catal. B Environ.* **2014**, *144*, 333–342. [CrossRef]
23. Peng, H.; Ying, J.; Zhang, J.; Zhang, X.; Peng, C.; Rao, C.; Liu, W.; Zhang, N.; Wang, X. La-doped Pt/TiO_2 as an efficient catalyst for room temperature oxidation of low concentration HCHO. *Chin. J. Catal.* **2017**, *38*, 39–47. [CrossRef]
24. Liu, H.; Yu, L.; Chen, W.; Li, Y. The Progress of TiO_2 Nanocrystals Doped with Rare Earth Ions. *J. Nanomater.* **2012**, *2012*, 235879. [CrossRef]
25. Chen, Y.; Wang, Y.; Li, W.; Yang, Q.; Hou, Q.; Wei, L.; Liu, L.; Huang, F.; Ju, M. Enhancement of photocatalytic performance with the use of noble-metal-decorated TiO_2 nanocrystals as highly active catalysts for aerobic oxidation under visible-light irradiation. *Appl. Catal. B Environ.* **2017**, *210*, 352–367. [CrossRef]
26. Momeni, M.M.; Akbarnia, M.; Ghayeb, Y. Preparation of S–W-codoped TiO_2 nanotubes and effect of various hole scavengers on their photoelectrochemical activity: Alcohol series. *Int. J. Hydrog. Energy* **2020**, *45*, 33552–33562. [CrossRef]
27. Wu, Y.; Zhang, J.; Xiao, L.; Chen, F. Properties of carbon and iron modified TiO_2 photocatalyst synthesized at low temperature and photodegradation of acid orange 7 under visible light. *Appl. Surf. Sci.* **2010**, *256*, 4260–4268. [CrossRef]
28. Sinhmar, A.; Setia, H.; Kumar, V.; Sobti, A.; Toor, A.P. Enhanced photocatalytic activity of nickel and nitrogen codoped TiO_2 under sunlight. *Environ. Technol. Innov.* **2020**, *18*, 100658. [CrossRef]
29. Lu, W.C.; Nguyen, H.D.; Wu, C.Y.; Chang, K.S.; Yoshimura, M. Modulation of physical and photocatalytic properties of (Cr, N) codoped TiO_2 nanorods using soft solution processing. *J. Appl. Phys.* **2014**, *115*, 144305. [CrossRef]
30. Liu, R.; Yang, F.; Xie, Y.; Yu, Y. Visible-light responsive boron and nitrogen codoped anatase TiO_2 with exposed {0 0 1} facet: Calculation and experiment. *Appl. Surf. Sci.* **2019**, *466*, 568–577. [CrossRef]

31. Jaiswal, R.; Bharambe, J.; Patel, N.; Dashora, A.; Kothari, D.C.; Miotello, A. Copper and Nitrogen co-doped TiO_2 photocatalyst with enhanced optical absorption and catalytic activity. *Appl. Catal. B Environ.* **2015**, *168*, 333–341. [CrossRef]
32. Zhang, S. Synergistic effects of C–Cr codoping in TiO_2 and enhanced sonocatalytic activity under ultrasonic irradiation. *Ultrason. Sonochem.* **2012**, *19*, 767–771. [CrossRef]
33. Patel, N.; Jaiswal, R.; Warang, T.; Scarduelli, G.; Dashora, A.; Ahuja, B.L.; Kothari, D.C.; Miotello, A. Efficient photocatalytic degradation of organic water pollutants using V–N-codoped TiO_2 thin films. *Appl. Catal. B Environ.* **2014**, *150*, 74–81. [CrossRef]
34. Trevisan, V.; Olivo, A.; Pinna, F.; Signoretto, M.; Vindigni, F.; Cerrato, G.; Bianchi, C.L. CN/TiO_2 photocatalysts: Effect of co-doping on the catalytic performance under visible light. *Appl. Catal. B Environ.* **2014**, *160*, 152–160. [CrossRef]
35. Cho, I.S.; Lee, C.H.; Feng, Y.; Logar, M.; Rao, P.M.; Cai, L.; Kim, D.R.; Sinclair, R.; Zheng, X. Codoping titanium dioxide nanowires with tungsten and carbon for enhanced photoelectrochemical performance. *Nat. Commun.* **2013**, *4*, 1723. [CrossRef]
36. Yang, X.; Ma, F.; Li, K.; Guo, Y.; Hu, J.; Li, W.; Huo, M.; Guo, Y. Mixed phase titania nanocomposite codoped with metallic silver and vanadium oxide: New efficient photocatalyst for dye degradation. *J. Hazard. Mater.* **2010**, *175*, 429–438. [CrossRef]
37. Devi, R.S.; Venckatesh, D.R.; Sivaraj, D.R. Synthesis of titanium dioxide nanoparticles by sol-gel technique. *Int. J. Innov. Res. Sci. Eng. Technol.* **2014**, *3*, 15206–15211. [CrossRef]
38. Vijayalakshmi, K.; Sivaraj, D. Synergistic antibacterial activity of barium doped TiO_2 nanoclusters synthesized by microwave processing. *RSC Adv.* **2016**, *6*, 9663–9671. [CrossRef]
39. Dahiya, M.S.; Tomer, V.K.; Duhan, S. Metal–ferrite nanocomposites for targeted drug delivery. In *Applications of Nanocomposite Materials in Drug Delivery*; Elsevier: Amsterdam, The Netherlands, 2018; pp. 737–760.
40. Badawi, A.; Althobaiti, M.G.; Alharthi, S.S.; Al-Baradi, A.M. Tailoring the optical properties of CdO nanostructures via barium doping for optical windows applications. *Phys. Lett. A* **2021**, *411*, 127553. [CrossRef]
41. Patel, S.; Gajbhiye, N.; Date, K.S. Ferromagnetism of Mn-doped TiO_2 nanorods synthesized by hydrothermal method. *J. Alloy. Compd.* **2011**, *509*, S427–S430. [CrossRef]
42. AlFaify, S.; Ganesh, V.; Haritha, L.; Shkir, M. An effect of La doping on physical properties of CdO films facilely casted by spin coater for optoelectronic applications. *Phys. B: Condens. Matter* **2019**, *562*, 135–140. [CrossRef]
43. N'Konou, K.; Lare, Y.; Haris, M.; Baneto, M.; Amou, K.A.; Napo, K. Influence of barium doping on physical properties of zinc oxide thin films synthesized by SILAR deposition technique. *Adv. Mater.* **2014**, *3*, 63–67. [CrossRef]
44. Cheng, G.; Xu, F.; Stadler, F.J.; Chen, R. A facile and general synthesis strategy to doped TiO_2 nanoaggregates with a mesoporous structure and comparable property. *RSC Adv.* **2015**, *5*, 64293–64298. [CrossRef]
45. Moss, T.S. The interpretation of the properties of indium antimonide. *Proc. Phys. Soc.* **1954**, *67*, 10. [CrossRef]
46. Singh, M.; Goyal, M.; Devlal, K. Size and shape effects on the band gap of semiconductor compound nanomaterials. *J. Taibah Univ. Sci.* **2018**, *12*, 470–475. [CrossRef]
47. Son, Y.; Park, M.; Son, Y.; Lee, J.S.; Jang, J.H.; Kim, Y.; Cho, J. Quantum confinement and its related effects on the critical size of GeO_2 nanoparticles anodes for lithium batteries. *Nano Lett.* **2014**, *14*, 1005–1010. [CrossRef] [PubMed]
48. Roth, A.; Webb, J.; Williams, D. Absorption edge shift in ZnO thin films at high carrier densities. *Solid State Commun.* **1981**, *39*, 1269–1271. [CrossRef]
49. Velusamy, P.; Babu, R.R.; Ramamurthi, K.; Elangovan, E.; Viegas, J. Effect of La doping on the structural, optical and electrical properties of spray pyrolytically deposited CdO thin films. *J. Alloy. Compd.* **2017**, *708*, 804–812. [CrossRef]
50. Chakraborty, P.; Datta, G.; Ghatak, K. The simple analysis of the Burstein–Moss shift in degenerate n-type semiconductors. *Phys. Condens. Matter* **2003**, *339*, 198–203. [CrossRef]
51. Kumar, R. Structural and optical studies of Mn^{2+} substituted CdO nano-particles. *Appl. Phys. A* **2021**, *127*, 249.
52. Kumar, K.C.; Rao, N.M.; Kaleemulla, S.; Rao, G.V. Structural, optical and magnetic properties of Sn doped ZnS nano powders prepared by solid state reaction. *Phys. B Condens. Matter* **2017**, *522*, 75–80. [CrossRef]
53. Sangiorgi, N.; Aversa, L.; Tatti, R.; Verucchi, R.; Sanson, A. Spectrophotometric method for optical band gap and electronic transitions determination of semiconductor materials. *Opt. Mater.* **2017**, *64*, 18–25. [CrossRef]
54. Reddy, K.M.; Manorama, S.V.; Reddy, A.R. Bandgap studies on anatase titanium dioxide nanoparticles. *Mater. Chem. Phys.* **2003**, *78*, 239–245. [CrossRef]
55. Yoo, K.; Kim, J.Y.; Lee, J.A.; Kim, J.S.; Lee, D.K.; Kim, K.; Kim, J.Y.; Kim, B.; Kim, H.; Kim, W.M.; et al. Completely transparent conducting oxide-free and flexible dye-sensitized solar cells fabricated on plastic substrates. *ACS Nano* **2015**, *9*, 3760–3771. [CrossRef] [PubMed]
56. Saeed, M.A.; Kang, H.C.; Yoo, K.; Asiam, F.K.; Lee, J.J.; Shim, J.W. Cosensitization of metal-based dyes for high-performance dye-sensitized photovoltaics under ambient lighting conditions. *Dye. Pigment.* **2021**, *194*, 109624. [CrossRef]
57. Amarsingh Bhabu, K.; Kalpana Devi, A.; Theerthagiri, J.; Madhavan, J.; Balu, T.; Rajasekaran, T.R. Tungsten doped titanium dioxide as a photoanode for dye sensitized solar cells. *J. Mater. Sci. Mater. Electron.* **2017**, *28*, 3428–3439. [CrossRef]